PHYSICAL REVIEW A **68**, 052502 (2003)

High-$|m|$ Rydberg states in strong magnetic fields

J. R. Guest and G. Raithel
FOCUS Center and Michigan Center for Theoretical Physics, Physics Department, University of Michigan,
Ann Arbor, Michigan 48109-1120, USA

(Received 9 December 2002; revised manuscript received 4 September 2003; published 11 November 2003)

We calculate spectra and wave functions of Rydberg atoms in strong magnetic fields using adiabatic basis sets, which reflect the different time scales of the electronic motion parallel and transverse to the magnetic field. For large absolute values of the azimuthal quantum number m, nonadiabatic corrections are found to be negligible, and the adiabatic basis states and their energies are exact solutions. With decreasing value of $|m|$, the system turns nonadiabatic, and the statistical behavior of the spectra changes from being consistent with classically regular to being consistent with classically chaotic motion. A relation describing the parameter region in which this transition occurs is obtained.

DOI: 10.1103/PhysRevA.68.052502 PACS number(s): 31.50.Gh, 36.20.Kd, 05.45.Mt, 32.60.+i

I. INTRODUCTION

Being a paradigm of ‘‘quantum chaos,’’ the diamagnetic hydrogen atom has been extensively investigated both in experiment and theory [1–3]. In the laboratory, such systems could be realized in the form of laser-excited Rydberg states in magnetic fields of the order of a few tesla. Most research on the field has dealt with subspaces of low values of the conserved magnetic quantum number $|m|$, because these subspaces are experimentally accessible through direct laser excitation, and because the classically chaotic dynamics predominantly occurs at low $|m|$. Experimental work began with the seminal discovery of quasi-Landau resonances in the Rydberg excitation spectra of atoms in strong magnetic fields [4]. In later work, more complex spectral modulations [5,6] were found. Level repulsion, a quantum indicator for classically chaotic dynamics, has been measured using lasers with a spectral resolution high enough to resolve individual Rydberg lines [7]. Unusually narrow resonances above the ionization limit have been observed [8], which were identified as positive-energy states in higher Landau bands [9,10]. Theoretical investigations, reviewed in Refs. [1–3], have included large-scale quantum-mechanical matrix calculations [11], adiabatic expansion methods that reflect the different time scales of the electronic motion transverse and parallel to the magnetic field [9,10], and semiclassical closed-orbit approximations, which are used for a multitude of problems [1–3,12]. The existing theoretical and experimental work provides a consistent and complete picture of quantum-classical correspondence in diamagnetic Rydberg atoms.

In the present paper, we investigate the properties of diamagnetic Rydberg states in the much less studied regime of *high* $|m|$. Low-lying states in this regime have been calculated by Delos *et al.* [13]. On grounds of the correspondence principle, the classical Rydberg-electron trajectories considered in Sec. II demonstrate that high-$|m|$ diamagnetic Rydberg states qualitatively differ from their low-$|m|$ counterparts. We continue in Sec. III with the description of a quantum-mechanical analysis of the bound states that is based on adiabatic basis sets. Our method is conceptually similar to the work presented in Refs. [9,10]. We use similar adiabatic basis sets as in Ref. [9], namely, the ones in which the adiabatic basis states are obtained in a transparent, straightforward manner via numerical integrations of one-dimensional Schrödinger equations for the fast and slow variables of the system. In contrast to the work in Ref. [9], we include the effects of all nonadiabatic corrections. In Ref. [10], different adiabatic basis sets were used and nonadiabatic corrections were included, but only low-$|m|$ manifolds were considered.

In our analysis of the obtained quantum spectra and wave functions, we show in Sec. IV that for large $|m|$ and B the Born-Oppenheimer approximation applies, i.e., the motions parallel and transverse to the magnetic field adiabatically separate. We then investigate typical nonadiabatic effects and study in detail how with decreasing $|m|$ the Born-Oppenheimer approximation breaks down. We thereby identify a quantitative condition on m and B that describes over which range the transition between adiabatic and nonadiabatic quantum behavior occurs. This is one of our main results. We then show in Sec. V that upon variation of $|m|$ from large to small values the energy-level statistics changes in a manner that is consistent with a transition from classically regular to chaotic dynamics. This ‘‘quantum-chaotic’’ transition is found to follow a classical scaling behavior governed by the same variable that also describes the degree of adiabaticity in the system.

The regularity and adiabatic separability of the system at large $|m|$ and B is not unexpected, because at large $|m|$ and B the Coulomb potential merely represents a weak, smooth perturbation to the problem of an electron in a homogeneous magnetic field (which is a separable problem). Further, our observation of a regular-to-chaotic transition upon variation of $|m|$ complements recent work on such transitions as a function of quantum defects [14].

Our work has been motivated by recent experiments on cold plasmas and cold Rydberg atom gases prepared in near-zero magnetic fields by the laser excitation of clouds of laser-cooled atoms. These experiments have revealed novel collisional dynamics [15–17]. It has, in particular, been found that high-angular-momentum Rydberg states can become populated through collisions or recombination. Fundamentally, an extension of cold-plasma research into the domain of strong magnetic fields appears critical, because the magnetic field is one of the most important parameters in any astrophysical, terrestrial, or man-made plasma. A strong magnetic field will increase the plasma lifetime, alter the plasma dynamics, and change the nature of any Rydberg atoms contained within the plasma. Further, due to the pinning of free charges to **B**-field lines, the addition of a strong magnetic field to cold plasmas is likely to suppress collisional electron heating mechanisms [18], potentially opening an avenue to the generation of a strongly coupled electron component in a cold plasma.

First steps towards high-B cold-plasma and Rydberg-gas research have been taken. We have recently been able to generate strongly magnetized cold plasmas and Rydberg atom gases in the laboratory [19]. Also, strongly magnetized cold plasmas are being considered in very recent theoretical work. With this emerging new direction in cold-plasma research comes a desire to calculate the quantum-mechanical properties of diamagnetic Rydberg states (lifetimes, transition rates, etc.). Thereby, high-$|m|$ states are particularly important because of their long lifetime and high density of states. We have already employed the method described in Sec. III of the present paper to calculate radiative lifetimes of strongly magnetized high-$|m|$ Rydberg states [20].

II. CLASSICAL DYNAMICS

Some intuition of what to expect when the magnetic quantum number $|m|$ is varied from small to large values can be obtained through classical trajectory calculations. We assume a magnetic field $\mathbf{B}=B\hat{\mathbf{z}}$. In the classical problem, the ‘‘good’’ magnetic quantum number m corresponds to the conserved z component of the canonical angular momentum $l_z=\hbar m$. At low $|m|$ and sufficiently high B and high energy, the Rydberg-electron trajectories are chaotic, while in the case of high $|m|$ apparently regular classical drift orbits exist. The drift orbits exhibit the same characteristics as charged-particle orbits in Penning traps, namely cyclotron, z-bounce, and magnetron oscillations [21,22]. The qualitatively different types of orbits are displayed in Fig. 1. The fact that for high $|m|$ the motion is composed of three components with quite different time scales was used as a justification to adiabatically separate the classical motion and to semiclassically quantize the system [21]. However, the exact quantum behavior and the role of nonadiabatic effects remained elusive in that approach.

Following the correspondence principle, which usually applies to Rydberg atoms, both the exact quantum states and the level spectra should reflect the existence of qualitatively different classical domains. This will be shown explicitly in Secs. IV and V. Concerning the choice of a method to treat the quantum-mechanical problem, it is obvious from Fig. 1 and earlier work in the field that it is most efficient to first solve the problem using a Born-Oppenheimer separation of the fast radial and the slow z-bounce motion. Even for low $|m|$, where quantum-chaotic signatures prevail, the adiabatic separation of the motions parallel and transverse to the **B** field has been found to be a fruitful approach [9].

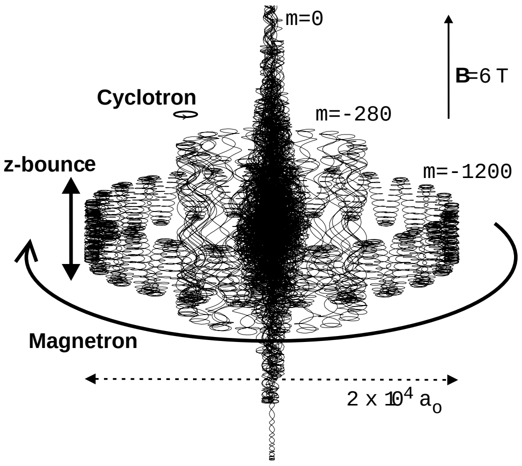

FIG. 1. Three classical trajectories of Rydberg electrons in a magnetic field $\mathbf{B}=(6\ \mathrm{T})\hat{\mathbf{z}}$ and energy $E=-5\times10^{-5}$ for the indicated values of the z component of the canonical angular momentum m (E and m in atomic units). The low-$|m|$ orbit is chaotic, while the high-$|m|$ orbits are regular and display the three indicated characteristic types of motion.

III. QUANTUM-MECHANICAL ANALYSIS

We use numerically obtained basis sets of adiabatic wave functions. These functions match the shape of the relevant potential, defined in Eq. (1) below, in an optimal manner, and therefore form ideal basis sets for the exact solution of the problem, giving good results even when the basis sets are small. We then calculate all nonadiabatic couplings, obtain exact solutions of the problem, and elaborate on the effects of the nonadiabatic couplings on the exact spectra and eigenstates.

Using an ansatz $\Psi(\mathbf{r})=(1/\sqrt{2\pi\rho})\psi(\rho,z)e^{im\phi}$, the Hamiltonian of a Rydberg atom with infinite nuclear mass in a magnetic field $\mathbf{B}=B\hat{\mathbf{z}}$ becomes, in atomic units, cylindrical coordinates, and in the symmetric gauge,

$$\hat{H}=-\frac{1}{2}\frac{\partial^2}{\partial\rho^2}-\frac{1}{2}\frac{\partial^2}{\partial z^2}+V(\rho,z)$$

with

$$V(\rho,z)=-\frac{1}{\sqrt{z^2+\rho^2}}+\frac{m^2-1/4}{2\rho^2}+\frac{B^2\rho^2}{8}+m\frac{B}{2}. \tag{1}$$

For large values of $|m|$, the potential $V(\rho,z)$ confines classical trajectories and quantum wave functions on thin and long cylindrical shells aligned with the **B** field, leading to regular classical motion with bounce frequencies much slower that the radial frequency, as manifested in Fig. 1. Therefore, it is advantageous to approach the problem via a Born-Oppenheimer separation of the ρ and z motions [9]. With the reduced Hamiltonian for the fast ρ motion, $\hat{H}_{\rho;z}=\hat{H}+\frac{1}{2}\partial^2/\partial z^2$, the eigenvalue equation for the ρ motion at fixed z reads

$$\hat{H}_{\rho;z}\psi_j(\rho;z)=U_j(z)\psi_j(\rho;z). \tag{2}$$

We numerically solve this equation for sets of about 5000 grid points of the z coordinate, and find the adiabatic potentials $U_j(z)$ and the corresponding radial functions $\psi_j(\rho;z)$. The $U_j(z)$ have minima at $z=0$, are symmetric in z, and asymptotically approach positive values. Since we are primarily interested in finding the bound states, we compute all adiabatic potentials $U_j(z)$ that satisfy $U_j(0)<0$ and are therefore likely to support bound states. Due to the constant Zeeman term $mB/2$ in Eq. (1), the number of potentials supporting bound states is larger for negative m than it is for positive m; therefore we focus on negative m. For a B field of 6 T and $|m|\geqslant 20$ we typically find 5–30 potentials with $U_j(0)<0$.

The solution of the Schrödinger equation for the slow motion,

$$\left(-\frac{1}{2}\frac{\partial^2}{\partial z^2}+U_j(z)\right)\xi_{jk}(z)=E_{jk}\xi_{jk}(z), \tag{3}$$

yields the adiabatic energies E_{jk} and the corresponding full adiabatic wave functions $\Psi(\mathbf{r})=(1/\sqrt{2\pi\rho})e^{im\phi}\psi_j(\rho;z)\xi_{jk}(z)$. Due to the symmetry of the $U_j(z)$, the solutions have well-defined z parity.

The adiabatic solutions $\psi_j(\rho;z)\xi_{jk}(z)$ are orthonormal and can be used to represent the exact Hamiltonian, Eq. (1), yielding matrix elements

$$\begin{aligned}H_{jk}^{j'k'}=&E_{jk}\delta_{jj'}\delta_{kk'}-\int_z\xi_{j'k'}(z)\left[\frac{d}{dz}\xi_{jk}(z)\right]\left(\int_\rho\psi_{j'}(\rho;z)\right.\\&\left.\times\left[\frac{\partial}{\partial z}\psi_j(\rho;z)\right]d\rho\right)dz-\frac{1}{2}\int_z\xi_{j'k'}(z)\xi_{jk}(z)\\&\times\left(\int_\rho\psi_{j'}(\rho;z)\left[\frac{\partial^2}{\partial z^2}\psi_j(\rho;z)\right]d\rho\right)dz,\end{aligned} \tag{4}$$

in which the integral terms represent the nonadiabatic couplings. One can explicitly show the symmetry of the nonadiabatic couplings in (j,k) and (j',k'). Further, due to the well-defined z parity of the adiabatic potentials $U_j(z)$, the functions $\xi_{jk}(z)$, and the functions $\psi_j(\rho;z)$, only nonadiabatic couplings between states with the same z parity exist, as required by the symmetry of the problem. Also, to reduce numerical computation errors we have used a modification of Eq. (4) in which only products of first-order z derivatives occur instead of the second-order z derivative [20]. The energies and eigenfunctions obtained via diagonalization of the matrix specified by Eq. (4) are exact up to basis truncation errors.

IV. TRANSITION FROM ADIABATIC TO NONADIABATIC BEHAVIOR

A. Energy-$\langle j\rangle$ diagrams

In this section, we discuss how with decreasing value of $|m|$ nonadiabatic couplings grow in importance and progressively lead to a reorganization of the spectra. In Fig. 2, we compare adiabatic with exact spectra for $B=6$ T and $m=-200$, -80, and -40. In the adiabatic spectra, we display the level series E_{jk} associated with the adiabatic potentials $U_j(z)$ in separated columns labeled by the radial adiabatic quantum number j. In the graphs of the exact energy levels, the discrete quantum number j is replaced by its quantum average $\langle j\rangle$. Thus, the energy-$\langle j\rangle$ diagrams of the exact spectra have an abscissa related to the average energy contained in the motion transverse to $\mathbf{B}$, while the ordinate represents the (total) level energy. The energy-$\langle j\rangle$ diagrams are a useful tool to study the transition from adiabatic to nonadiabatic behavior. The diagrams are also found to highlight structures that are due to quantum-classical correspondence.

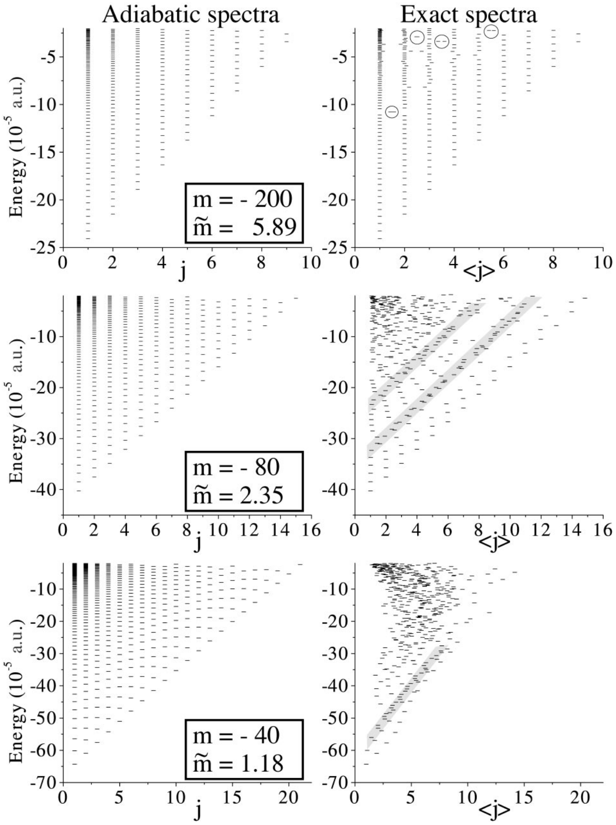

FIG. 2. Adiabatic (left) and exact energy levels (right) for $B=6$ T, even z parity, energy $E<-2\times10^{-5}$, and the indicated values of m and $\tilde{m}$. The circles in the upper right panel indicate a few isolated nonadiabatic state-mixing events. The accumulations of exact levels along diagonal lines, highlighted by gray shadings and most clearly visible in the case $\tilde{m}=2.35$, are due to resonances of the ρ and z motion, as discussed in the text.

To quantify the degree of adiabaticity, we use a parameter related to the ratio between the radial and z-oscillation frequencies ω_ρ and ω_z. In the regime of moderate to high $|m|$, the value of ω_ρ is approximately given by the cyclotron frequency, which in atomic units equals B. The value of ω_z is obtained by expanding the potential in Eq. (1) around $z=0$ for a fixed radial coordinate ρ_0. A suitable choice for ρ_0 is the radial coordinate of the potential minimum for $|z|\rightarrow\infty$. The adiabaticity parameter $\tilde{m}$ we use is defined by

$$\tilde{m}=\frac{1}{2}\left(\frac{\omega_c}{\omega_z}\right)^{4/3}=|m|B^{1/3}. \tag{5}$$

We use this specific function because it turns out to be identical with the (classical) scaled z-angular momentum of the system employed in Sec. V. For the cases $m=-200$, -80, and -40 of Fig. 2, the adiabaticity parameters are $\tilde{m}=5.89$, 2.35, and 1.18.

B. Adiabatic regime

For $\tilde{m}=5.89$, the adiabatic and exact spectra are virtually identical, showing that for this $\tilde{m}$ the nonadiabatic couplings are generally weak and that most exact states are dominated by a single adiabatic basis state. Thus, the Born-Oppenheimer approximation is clearly valid when $\tilde{m}$ is of the order of six or larger. The classical analogs of exact quantum states in the adiabatic regime are orbits such as the outer two in Fig. 1.

In the adiabatic regime, nonadiabatic state mixing only occurs when two adiabatic states are accidentally near degenerate. In that case, adiabatic states with quantum numbers j and j' become mixed and generate exact levels with values $\langle j \rangle$ and $\langle j' \rangle$ that are closer together the closer the near degeneracy is. An inspection of the upper-right panel of Fig. 2, where a few distinguishable and isolated mixing events are identified, shows that in the adiabatic regime there exists an approximate selection rule for nonadiabatic state mixing: mixing is seen to occur mostly between near-degenerate adiabatic states with j numbers differing by one. This selection rule can be traced to the relative importance of the (embedded) radial integrals in Eq. (4). For fixed z, the dependence of the potential $V(\rho,z)$ in Eq. (1) on ρ is fairly harmonic in the vicinity of the radial potential minimum. Further, the z dependence of the radial wave functions $\psi_j(\rho;z)$ mostly consists of a slight translation in ρ that is linear in z, as evidenced by the wave function plots in Fig. 3. Thus, $(\partial/\partial z)\psi_j(\rho;z)\approx \pm\alpha(\partial/\partial\rho)\psi_j(\rho;z)$, where α is the amount of radial translation of ψ_j per z interval. The direction of the linear shift, i.e., the sign in front of α, equals the sign of z. Considering the properties of the wave functions of the quantum harmonic oscillator, it is seen that $(\partial/\partial z)\psi_j(\rho;z)$ approximately yields $\pm\alpha$ times a linear combination of $\psi_{j+1}(\rho;z)$ and $\psi_{j-1}(\rho;z)$. As a result, the first radial integral in Eq. (4) becomes large only if the j numbers of the involved states differ by one. Further considerations show that the second (embedded) radial integral in Eq. (4), which involves a $(\partial^2/\partial z^2)\psi_j(\rho;z)$ and would yield mixing between adiabatic levels with j numbers differing by two, provides smaller contributions. In this way, the dominance of nonadiabatic couplings between states with j numbers differing by one, as seen for $\tilde{m}=5.89$ in Fig. 2, can be explained.

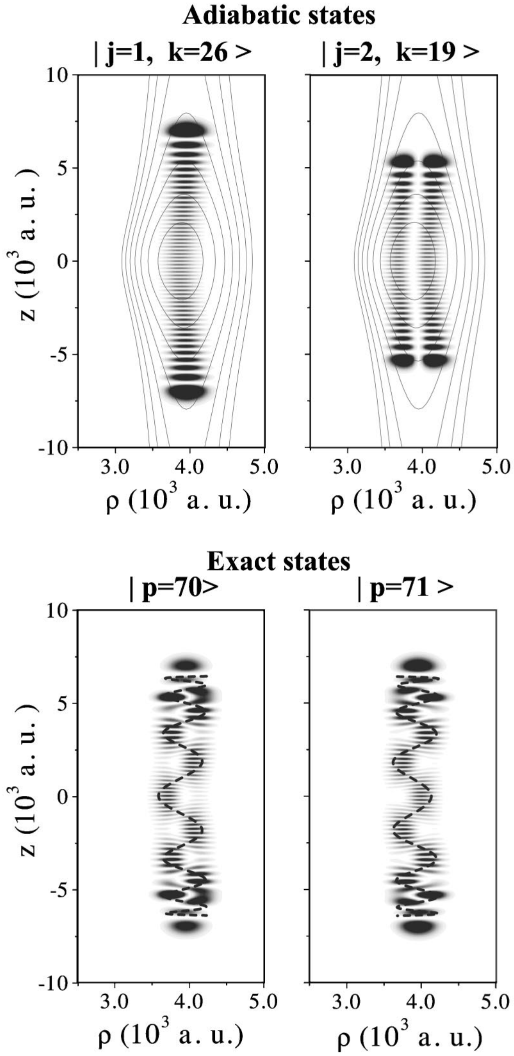
Adiabatic states

| j=1, k=26 >

| j=2, k=19 >

Exact states

| p=70>

| p=71 >

FIG. 3. A case of exceptionally strong nonadiabatic coupling of $m=-200$ states in Fig. 2. The figure shows gray scale representations of wave function probabilities in the ρz plane. On the left pair of panels, the wave functions of the accidentally near-degenerate adiabatic states $|j=1,k=26\rangle$ and $|j=2,k=19\rangle$ are displayed. The adiabatic states become mixed by virtue of the nonadiabatic coupling term $H^{j=1,k=26}_{j=2,k=19}$ in Eq. (4). The exact calculation yields a pair of quantum states that are near-degenerate linear superpositions of the adiabatic states $|j=1,k=26\rangle$ and $|j=2,k=19\rangle$. In the depicted case, the mixed exact states are labeled $|p=70\rangle$ and $|p=71\rangle$, according to rank in energy value. In the upper-right panel of Fig. 2, the states $|p=70\rangle$ and $|p=71\rangle$ are located in the lowest circle. The equipotential lines of the potential in Eq. (1) are shown in the left pair of panels. Note the different scales in ρ and z. Further, note that an adiabatic state $|j,k\rangle$ denotes the $(2k-1)$th z-bounce state with radial quantum number j, because our calculations are for states with even z parity. The dashed lines superimposed on the exact quantum states are classical periodic trajectories calculated for an energy equal to that of the quantum states.

One of these nonadiabatic mixing events marked in the upper-right panel of Fig. 2 is investigated more closely in Fig. 3. There, the z-dependent variations of the average radial coordinates of the adiabatic wave functions, the derivatives of which yield the value of α used in the preceding paragraph, present a qualitative measure for the strength of the nonadiabatic coupling. Since these variations are very slight, the nonadiabatic coupling is small and only leads to noticeable state mixing because of the near-degeneracy of the involved adiabatic levels. The wave functions of the mixed states are localized around classical periodic trajectories, as indicated by the dashed lines in Fig. 3. The periodic trajectories correspond to resonances of the ρ and z motion: during one z-bounce oscillation an integer number of radial oscillations occur. The example in Fig. 3 and other cases we have studied suggest that the few, isolated cases of nonadiabatic state mixing that occur in the adiabatic regime coincide with resonances of the classical ρ and z motion. This finding conforms with the commonly known fact that nonadiabatic effects are maximal if there is a resonance between the motions in the relevant degrees of freedom.

C. Transition regime

With decreasing value of $\tilde{m}$, the exact spectra in Fig. 2 deviate farther from the adiabatic spectra, signaling the breakdown of the Born-Oppenheimer approximation. In the energy-$\langle j\rangle$ diagrams, two distinct regimes of nonadiabatic behavior can be identified. As $\tilde{m}$ is decreased, the arrangement of exact energy levels in the energy-$\langle j\rangle$ diagrams first changes from largely adiabatic ($\tilde{m}=5.89$ in Fig 2) into a transitional pattern in which a fraction of energy levels still follows an arrangement similar to the adiabatic scheme, a second fraction of levels accumulates along diagonal lines in the energy-$\langle j\rangle$ plane, and a third fraction appears to be randomly distributed. In Fig. 2, the case $\tilde{m}=2.35$ exhibits a typical transitional pattern. As $\tilde{m}$ is lowered further, the fraction of randomly distributed levels becomes overwhelmingly dominant. In the following, we focus on the second fraction of energy levels, which is most prominent in the transitional regime.

Already in the adiabatic case $\tilde{m}=5.89$ in Fig. 2, the scattered nonadiabatic coupling events seem to be arranged along virtual diagonal lines through the energy-$\langle j\rangle$ plane. As the adiabaticity parameter $\tilde{m}$ is lowered, the manifestations of nonadiabatic couplings become more widespread in the spectra and begin to mix adiabatic states with j numbers differing by more than one. It also becomes obvious that nonadiabatic effects do, in fact, nucleate along diagonal virtual lines through the energy-$\langle j\rangle$ plane, as indicated by the shaded regions in Fig. 2. This behavior is clearly observed in the case $\tilde{m}=2.35$ of Fig. 2, where in certain energy ranges nonadiabatic couplings lead to the accumulation of 30–50 % of all energy levels along such virtual lines. It turns out that each such line marks a well-defined resonance between the ρ and the z motion. Since nonadiabatic effects are expected to first manifest themselves on such resonances, the observed nucleation behavior of nonadiabatic effects is expected. In the following, it is explained why so many energy levels accumulate on the virtual lines.

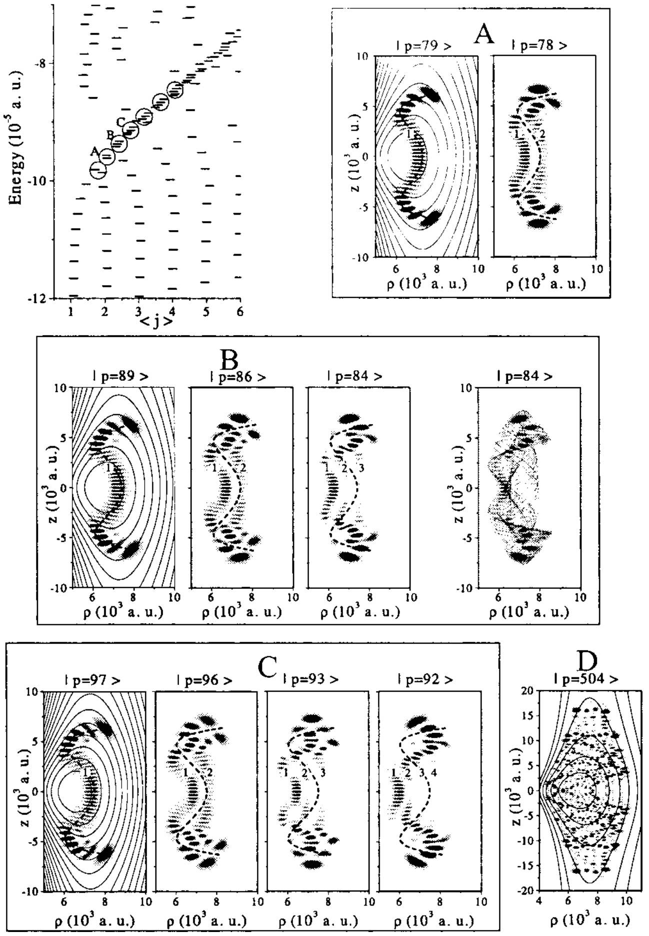

FIG. 4. Exact energy levels vs $\langle j\rangle$ and plots of the wave functions of the encircled and labeled level groups for $B=1$ T and $m=-120$. The p-quantum numbers of the wave functions refer to rank in energy value. The members of each group are sorted according to the number of wave-function maxima transverse to the displayed periodic orbit, which generates the sequence. The transverse maxima are labeled through by the numbers imprinted on the wave functions. The contour lines of the potential in Eq. (1) are, for clarity, only shown with the fundamental group members. The repeated plot of state $|p=84\rangle$ on the right of group B demonstrates that wave-function anomalies are connected with focal points and caustics of corresponding classical trajectories. The wave function of the randomly selected high-lying state $|p=504\rangle$ corresponds to a classically chaotic portion of phase space.

We will first point out that the accumulation of energy levels along virtual lines in the energy-$\langle j\rangle$ plane follows certain patterns. Since these patterns are most easily recognized in systems with a large density of states, we discuss an example at a lower magnetic field $B=1$ T and $m=-120$ (i.e., $\tilde{m}=1.94$). The physics of this case is similar to that of the case $\tilde{m}=2.35$ in Fig. 2, but the average density of states is considerably higher. We show in Fig. 4 a detail of the spectrum for $B=1$ T and $m=-120$ represented in the energy-$\langle j\rangle$ plane. The line along which energy levels accumulate corresponds to the 1:4 resonance (i.e., four radial oscillations per z oscillation). As indicated in the figure by circles, in a certain energy range the levels are systematically organized in groups. These level patterns are significant, in that they can be associated with a reproducible, well-defined behavior of the associated wave functions. This is demonstrated by plotting the wave functions of three level groups, labeled A, B, and C in Fig. 4. The wave functions of the highest levels within the groups clearly follow the periodic orbit that corresponds to the 1:4 resonance, and do not have any significant structure transverse to the orbit. Thus, the wave functions of the highest levels within the groups can be regarded as the fundamental wave functions of the groups. The wave functions with the second-highest energies within the groups are arranged around the same orbit as the fundamental wave functions, while exhibiting—in most of their parts—one node in the direction transverse to the orbit. For the next-lower levels, we tend to observe two nodes transverse to the orbit, and so on (see numbers imprinted on the wave function plots of Fig. 4).

The observed quantization structure corresponds with sets of invariant tori centered around a stable periodic orbit. In the case of Fig. 4, the periodic orbit is that of the 1:4 resonance. The (semiclassical) density of quantum states associated with the set of tori is approximately proportional to the energy derivative of the phase-space volume of the set of tori. We have calculated Poincare surfaces of section for the parameters of Fig. 4, and estimated that the semiclassical density of states of the torus set belonging to the 1:4 resonance can approach 50% of the total density of states. This explains why in the energy-$\langle j\rangle$ diagram in Fig. 4 so many states accumulate on the line corresponding to the 1:4 resonance.

For quantitative studies of the quantum states on the invariant tori, one may employ the well-known theory of multidimensional semiclassical quantization of regular systems, which is reviewed by Gutzwiller [2]. In the present energy-conserving two-dimensional case, the ‘‘allowed’’ invariant tori are characterized by the action integrals along two topologically different closed loops in phase space, each of which generates a semiclassical quantum number. In our case, one of these integrals is related to a longitudinal quantum number, which one may define as the number of wave-function maxima along a line that is parallel to the underlying periodic orbit. In Fig. 4, the assignment of longitudinal quantum numbers to the fundamental wave functions is straightforward. It is observed that from one fundamental wave function to the next-higher one the longitudinal quantum number increases by two. This increment is to be expected, because we are only considering states with even z parity, which must all have an antinode in the $z=0$ plane.

For the wave functions with excitations transverse to the underlying periodic orbit, the assignment of longitudinal quantum numbers is somewhat complicated, because the nodal lines of these wave functions do not follow simple grid patterns of curves parallel and transverse to the orbit, but incorporate multiple abnormal structures. To explain the origin of these complications, in the plot on the right of the B group in Fig. 4 we show a trajectory superimposed on the wave function of the second transverse excitation of the B group. The trajectory is the configuration-space projection of a phase-space orbit located on an invariant torus that is centered around the 1:4 resonance of the radial and the z motion. First, we observe a striking similarity between the overall shape of the wave function and the area covered by the trajectory. Further, the trajectory displays multiple focal points, which mostly correspond to regions of enhanced wave-function amplitudes. Also, at the focal spots additional ‘‘waves’’ are inserted into the wave function, as is most clearly observed at the focus in the $z=0$ plane. Such additional waves must be expected due to Maslov indices associated with focal points. These and other observations make us confident that the invariant torus on which the displayed trajectory is located is fairly close to the one that, in a strict sense, corresponds to the second transverse excitation of the B group. However, the wave-function irregularities associated with the focal points of the displayed trajectory complicate the assignment of a longitudinal quantum number. Additional complications arise due to the nontrivial structure of the wave function near the caustics of the trajectory. For these reasons, we do not assign longitudinal quantum numbers to the wave functions in Fig. 4.

The second action integral characterizing the allowed invariant tori around the 1:4 resonance is associated with a transverse quantum number, which one may define as the number of wave-function maxima transverse to the underlying periodic orbit. For the wave functions in Fig. 4, the assignment of transverse quantum numbers is fairly obvious. Note, however, that portions of the wave functions clearly show the complicating effect of focal points and caustics of trajectories on both the longitudinal and the transverse structure of the wave functions.

It will be possible to quantitatively reproduce the quantization structure displayed in Fig. 4 by multidimensional semiclassical quantization on invariant tori [2]. Such an effort is beyond the scope of the present paper, but it may be the subject of future work. We close this discussion by pointing out that the influence of classical trajectories on quantum systems has, in general, been extensively studied [1–3,12], and that there is a large amount of literature one can work from.

For our purpose, an important aspect is that the breakdown of the Born-Oppenheimer separation of radial and z motion does not immediately lead to a fully chaotic behavior. With decreasing $\tilde{m}$, the course of events in the classical system is that the simple structure of invariant tori present in the fully adiabatic case ($\tilde{m}\gtrsim 6$) gradually breaks up, giving way to growing chaotic phase-space domains and new regular phase-space domains. The latter are filled with new sets of invariant tori centered around stable periodic orbits of the system. The new sets of invariant tori have clear manifestations in the quantum spectra and the wave functions, as we have seen in this section. With decreasing $\tilde{m}$, the chaotic fraction of classical phase space increases from ~ 0 at $\tilde{m}=6$ to $\lesssim 100\%$ at $\tilde{m}=1$, as we have verified by inspecting Poincare surfaces of section (not shown in this paper). The described transitional behavior occurs throughout a rather wide range of the adiabaticity parameter ($6\gtrsim\tilde{m}\gtrsim 1$).

D. Nonadiabatic chaotic regime

As discussed in the preceding section, the energy-$\langle j\rangle$ diagrams allow us to distinguish between two distinct types of nonadiabatic domains. In the domain considered in Sec. IV C, the adiabatic quantization structure is replaced by a regular quantization structure generated by sets of invariant tori around the stable periodic orbits of the system. The other domain of nonadiabatic behavior corresponds to the portions in the energy-$\langle j\rangle$ diagrams in which the energy levels appear to be disorganized. The latter domain becomes particularly prominent for $\tilde{m} \lesssim 3$, high energy, and low $\langle j \rangle$. Typically, wave functions of levels located in the disorganized portions of the energy-$\langle j \rangle$ diagrams are mixtures of many adiabatic states, and lack any regular node pattern or (obvious) alignment with classical trajectories. As a typical example of such wave functions, in group D of Fig. 4 we show the wave function of the level $|p=504\rangle$, which has been randomly picked from the disorganized portion of the energy-$\langle j \rangle$ diagram at $B=1$ T and $m=-120$. The disorganized portions in the energy-$\langle j \rangle$ diagrams expand with decreasing $\tilde{m}$; in the case $\tilde{m}=1.17$ of Fig. 2, almost the whole energy-$\langle j \rangle$ diagram is disorganized. Based on the discussion at the end of Sec. IV C, it is obvious that the described phenomenology of the energy-$\langle j \rangle$ diagrams and the widespread appearance of wave functions such as the "chaotic" state $|p=504\rangle$ in Fig. 4 reflect a regular-to-chaotic transition of the classical system. In the following section, we show that the statistical behavior of the quantum energy levels conforms with this assessment.

V. LEVEL STATISTICS

In the remainder of the paper, we study the variation of statistical properties of the spectra with B and $|m|$. The strength of the mixing of the adiabatic basis states and the concomitant level repulsion can be quantitatively measured via the probability distribution P of the nearest-neighbor energy splittings in the spectra, which is also known to reflect the nature of the dynamics of the corresponding classical system [1–3]. A Poissonian distribution indicates classically regular dynamics, while a Wigner distribution indicates chaotic dynamics. Since the average density of states strongly varies as a function of the energy E, we use a mapping function $S(E)$ defined such that the mapped values $\{S(E_n)\}$ of the quantum spectrum $\{E_n\}$ have a constant average nearest-neighbor separation of one on the S scale. The function $S(E)$ is given by the leading term of the semiclassical number of quantum states with energy $<E$. In atomic units and for the two-dimensional case of interest, it is

$$S(E)=\frac{1}{2}\,\frac{1}{2\pi}\int_0^{E-E_{\min}} A(E-E')\,dE', \qquad (6)$$

where the factor 1/2 accounts for the fact that we only consider states with even z parity. The integration variable E' is the kinetic energy, and $E_{\min}$ is the minimum energy of $V(\rho,z)$ from Eq. (1). The variable $A(E-E')$ represents the area in the ρz plane where $V(\rho,z)<E-E'$,

$$A(E-E')=\int_{V(\rho,z)<E-E'} dz\,d\rho. \qquad (7)$$

For $B=6$ T and all subspaces of m ranging from -20 to -450, we have computed the quantum spectra $\{E_n\}$. The utilized adiabatic basis sets were truncated at an energy -2×10^{-5}. From the spectra $\{E_n\}$ we have derived the corresponding mapped spectra $\{S_n=S(E_n)\}$ and their probability distributions $P(s)$ for the nearest-neighbor separations s of the S values. $P(s)$ have been obtained for both the adiabatic spectra, i.e., the eigenvalues obtained by solving Eq. (3), and for the exact spectra, i.e., the eigenvalues obtained by diagonalizing the matrix with elements defined in Eq. (4). To improve the statistics, the respective distributions $P_{\rm ad}(s)$ and $P_{\rm ex}(s)$ have then been averaged over small ranges of m that have a full width of about 12% of their average m. This width is large enough to yield reasonably smooth m-averaged distributions $\tilde{P}_{\rm ad}(s)$ and $\tilde{P}_{\rm ex}(s)$, while being small enough that the individual distributions contributing to the averages do not vary significantly. In Fig. 5, we show a few plots of $\tilde{P}_{\rm ad}(s)$ and $\tilde{P}_{\rm ex}(s)$.

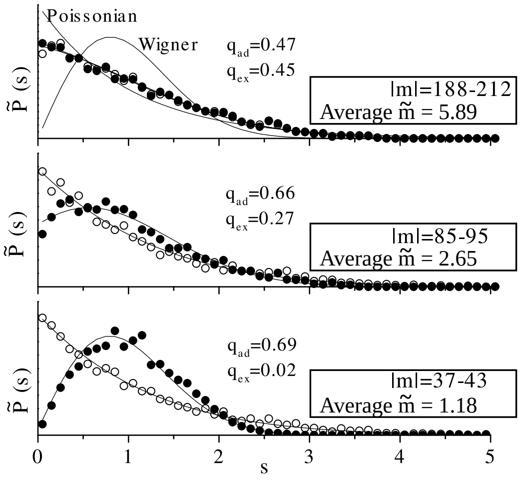

FIG. 5. Distributions $\tilde{P}_{\rm ad}(s)$ (open circles) and $\tilde{P}_{\rm ex}(s)$ (filled circles) of nearest-neighbor energy splittings for the indicated ranges of $|m|$ and $B=6$ T. The values $q_{\rm ad}$ ($q_{\rm ex}$) and lines show the respective q-fit results according to Eq. (8). In the uppermost panel we show, for reference, a perfect Poissonian ($q=0$) and a Wigner ($q=1$) distribution.

A quantitative figure for how Poisson- or Wigner-like a distribution $P(s)$ is can be obtained by fitting $P(s)$ with functions of the type [23]

$$P(s,q)=q^2e^{-qs}\,\mathrm{erfc}\left(\tfrac{1}{2}\sqrt{\pi}q's\right)+\left(2qq'+\tfrac{1}{2}\pi q'^3 s\right)\times e^{-qs-(1/4)\pi q'^2 s^2}. \qquad (8)$$

with $q'=1-q$. The fit parameter q is 1 for a pure Poissonian, 0 for a Wigner distribution, and varies between 0 and 1 for mixed distributions. Berry and Robnik [23] have shown that Eq. (8) yields a quite generally correct description of $P(s)$ for systems such as ours (two-dimensional systems with one dominant chaotic domain in classical phase space). In Fig. 5, we show the fits of all distributions with functions of the type of Eq. (8).

In Fig. 5, all $\tilde{P}_{\rm ad}(s)$ appear Poissonian. This is expected, as under the neglect of the nonadiabatic couplings the total spectrum is merely the sum of overlapping and independent series of z-bounce energy levels, each series being generated by a single adiabatic potential $U_j(z)$. Nearest neighbors in the total spectra generally belong to different series, and their separations tend to be random. One can also argue that, if the Born-Oppenheimer approximation were truly accurate, as

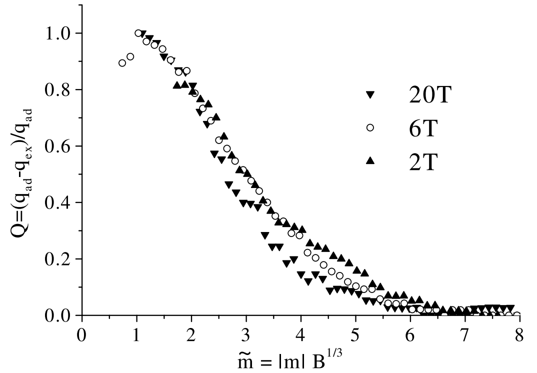

FIG. 6. Variation of the Q parameter defined in the text vs scaled z-angular momentum $\tilde{m}$ for $B=2$ T, 6 T, and 20 T.

implied by neglecting the nonadiabatic couplings, the underlying classical system would be adiabatically separable and thus regular. The corresponding quantum spectrum would thus exhibit a Poissonian distribution.

The q-fit results for the $\tilde{P}_{\mathrm{ad}}(s)$, shown in Fig. 5, deviate from the ideal Poissonian value 1. The deviation grows with increasing $|m|$ and B. Regarding this behavior, we first note that the q fits according to Eq. (8) are quite biased towards $q=0$, i.e., a minor deviation of $\tilde{P}_{\mathrm{ad}}(s)$ from a Poissonian already leads to a large departure of q from 1. Further, it has been found before that quantum systems with classically regular analogs may have distributions $P(s)$ that deviate from Poissonians [11]. The deviations that occur in our case are apparently due to the fact that the adiabatic spectra contain only a limited number of z-bounce energy level series, as seen in Fig. 2. The number of series decreases with increasing $|m|$ and B, leading to an increasing amount of correlations in the adiabatic spectra, and thus to increasing deviations of $\tilde{P}_{\mathrm{ad}}(s)$ from Poissonians.

Figure 5 demonstrates that, as the adiabaticity parameter $\tilde{m}$ is decreased, the distributions $\tilde{P}_{\mathrm{ex}}(s)$ turn from Poisson-like to Wigner-like. The change reflects the growing importance of the nonadiabatic couplings with decreasing $\tilde{m}$. Larger nonadiabatic couplings cause stronger level repulsions and thus more Wigner-like distributions $\tilde{P}_{\mathrm{ex}}(s)$. As generally accepted, this change in $\tilde{P}_{\mathrm{ex}}(s)$ reflects a corresponding change of the dynamics of the analogous classical system from regular to chaotic.

In the present classical system, the introduction of scaled variables [1,3] (scaled position $\mathbf{r}_s=\mathbf{r}B^{2/3}$, scaled canonical momentum $\mathbf{p}_s=\mathbf{p}B^{-1/3}$, scaled energy $\epsilon=EB^{-2/3}$, and scaled z-angular momentum $\tilde{m}=|m|B^{1/3}$) allows one to eliminate the magnetic field from the classical equations of motion, thereby reducing the number of system parameters from three (energy, B field, and z-angular momentum) to two (scaled energy and scaled z-angular momentum). The energy-averaged classical behavior is then solely determined by the scaled z-angular momentum, which is identical with the adiabaticity parameter defined in Eq. (5).

Since the Poisson- to Wigner-like transition of the $\tilde{P}_{\mathrm{ex}}(s)$ reflects the transition of classical behavior from regular to chaotic, the Poisson-to-Wigner transition of the quantum spectra should follow the classical scaling property, i.e., the transition should occur at a fixed value of the classical variable $\tilde{m}$. To verify the relevance of the classical scaling property of the system to the statistical behavior of its quantum energy levels, we have obtained and fit numerous distributions $\tilde{P}_{\mathrm{ad}}(s)$ and $\tilde{P}_{\mathrm{ex}}(s)$ for $B=2$ T, 6 T, and 20 T. In Fig. 6, we show the quantity $Q=(q_{\mathrm{ad}}-q_{\mathrm{ex}})/q_{\mathrm{ad}}$ assembled from the respective q-fit results vs $\tilde{m}$. Thereby, the (empirical) form of Q used should eliminate the above noted systematic variation of q_{ad} with $|m|$ and B.

From the agreement of all curves in Fig. 6 we conclude that classical scaling applies, and that the transition from chaotic-to-regular dynamics largely occurs between $\tilde{m}=1$ and 6, with most of the change happening in the range $2<\tilde{m}<4$. This is the same range over which the system turns from adiabatic to nonadiabatic. Chaotic dynamics occurs only up to a critical value $\tilde{m}\approx 6$. The majority of classical phase space exhibits regular dynamics when integrated over $\tilde{m}$. Quantitatively, we have estimated that for $B=6$ T and energies below -5×10^{-5} (i.e., only counting states more strongly bound than an $n=100$ state at $B=0$) state of the order of 50 000 exist in the largely chaotic domain, and about the same number in the largely regular domain. Raising the maximum energy of counted states or increasing the B field shifts the level-count balance to the regular domain.

VI. CONCLUSION

We have studied the spectra of high-$|m|$ Rydberg atoms in strong magnetic fields as a function of an adiabaticity parameter $\tilde{m}=|m|B^{1/3}$, and found that for $\tilde{m}\gtrsim 6$ the dynamics parallel and transverse to the magnetic field adiabatically separate. This finding justifies *a posteriori* the approximations we have made in previous semiclassical calculations [21]. We have then investigated the effects of nonadiabatic couplings on quantum spectra and wave functions, and found that the system undergoes a change from adiabatic to fully nonadiabatic behavior over a range $6\gtrsim\tilde{m}\gtrsim 1$. We have used a different representation of energy levels on the energy-$\langle j\rangle$ plane, which has allowed us to identify adiabatic and two distinct nonadiabatic domains. Prominent structures in the energy-$\langle j\rangle$ diagrams could be explained using quantum-classical correspondence. Finally, the probability distribution of nearest-neighbor energy splittings has been shown to exhibit a regular-to-chaotic transition over the range $6\gtrsim\tilde{m}\gtrsim 1$. In our considerations, the variable $\tilde{m}$ has served two distinct purposes: First, as an adiabaticity parameter suited to describe the transition between adiabatic and nonadiabatic regimes, and, second, as a scaled variable of the classical equations of motion suited to delineate classically regular and chaotic regimes. The twofold significance of $\tilde{m}$ explicitly highlights the intimate relationship between the breakdown of the Born-Oppenheimer approximation and the regular-to-chaotic transition.

Under experimental conditions where strongly magnetized Rydberg states are populated according to their density of states and lifetimes, not according to optical selection rules, the adiabatically separable high-$|m|$ states will become significantly populated. We expect that such conditions will occur in cold, strongly magnetized plasmas, which is an emerging field in experimental physics. It is likely that the accurate modeling of experiments on this field will require theoretical data on strongly magnetized high-$|m|$ Rydberg states. We have already used the presented methods to calculate radiative lifetimes [20]. In the future, we intend to calculate rf transition strengths, collision cross sections, and laser-induced recombination rates of strongly magnetized high-$|m|$ Rydberg states.

ACKNOWLEDGMENTS

We acknowledge the support by the Chemical Sciences, Geosciences and Biosciences Division of the Office of Basic Energy Sciences, Office of Science, U.S. Department of Energy.

---

[1] H. Friedrich and D. Wintgen, Phys. Rep. **183**, 37 (1989), and references therein.
[2] M.C. Gutzwiller, *Chaos in Classical and Quantum Mechanics* (Springer, New York, 1990), and references therein.
[3] H. Friedrich, *Theoretical Atomic Physics* (Springer, New York, 1991), and references therein.
[4] W.R.S. Garton, F.S. Tomkins, Astrophys. J. **158**, 839 (1969); A.F. Starace, J. Phys. B **6**, 585 (1973).
[5] A. Holle *et al.*, Phys. Rev. Lett. **56**, 2594 (1986); J. Main *et al.*, *ibid.* **57**, 2789 (1986); G. Wiebusch *et al.*, *ibid.* **62**, 2821 (1989).
[6] G. Raithel, M. Fauth, and H. Walther, Phys. Rev. A **44**, 1898 (1991).
[7] H. Held, J. Schlichter, G. Raithel, and H. Walther, Europhys. Lett. **43**, 392 (1998); K. Karremans, W. Vassen, W. Hogervorst, Phys. Rev. Lett. **81**, 4843 (1998).
[8] C. Iu *et al.*, Phys. Rev. Lett. **66**, 145 (1991).
[9] Q. Wang and C.H. Greene, Phys. Rev. A **40**, 742 (1989).
[10] S. Watanabe and H.A. Komine, Phys. Rev. Lett. **67**, 3227 (1991).
[11] D. Delande and J.C. Gay, Phys. Rev. Lett. **57**, 2006 (1986); D. Wintgen and H. Friedrich, *ibid.* **57**, 571 (1986); G. Wunner *et al.*, *ibid.* **57**, 3261 (1986).
[12] See, for instance, M.C. Gutzwiller, J. Math. Phys. **8**, 1979 (1967); **10**, 1004 (1969); **11**, 1791 (1970); **12**, 343 (1971); M.C. Gutzwiller, Physica D **5**, 183 (1982); M.L. Du and J.B. Delos, Phys. Rev. A **38**, 1896 (1988); **38**, 1913 (1988); E.J. Heller, Phys. Rev. Lett. **53**, 1515 (1983); E.B. Bogomolny, Physica D **31**, 169 (1988).
[13] J.B. Delos *et al.*, Phys. Rev. A **37**, 4582 (1988).
[14] T.S. Monteiro and G. Wunner, Phys. Rev. Lett. **65**, 1100 (1990); M. Courtney and D. Kleppner, Phys. Rev. A **53**, 178 (1996); T. Jonckheere, B. Grémaud, and D. Delande, Phys. Rev. Lett. **81**, 2442 (1998); K. Karremans *et al.*, Phys. Rev. A **60**, R2649 (1999).
[15] S. Dutta *et al.*, Phys. Rev. Lett. **86**, 3993 (2001).
[16] T.C. Killian *et al.*, Phys. Rev. Lett. **86**, 3759 (2001).
[17] T.C. Killian *et al.*, Phys. Rev. Lett. **83**, 4776 (1999); S. Kulin *et al.*, *ibid.* **85**, 318 (2000); M.P. Robinson *et al.*, *ibid.* **85**, 4466 (2000).
[18] F. Robicheaux and J.D. Hanson, Phys. Rev. Lett. **88**, 055002 (2002).
[19] J.R. Guest, J.-H. Choi, A.P. Povilus, and G. Raithel (unpublished).
[20] J.R. Guest, J.-H. Choi, and G. Raithel, Phys. Rev. A **68**, 022509 (2003).
[21] G. Raithel and M. Fauth, J. Phys. B **28**, 1687 (1995).
[22] L.S. Brown and G. Gabrielse, Rev. Mod. Phys. **58**, 233 (1986), and references therein.
[23] M.V. Berry and M. Robnik, J. Phys. A **17**, 2413 (1984).